









Fluctuating Ru trimer precursor to a two-stage electronic transition in RuP

Robert J. Koch,¹ Niraj Aryal¹,,¹ Oleh Ivashko²,,² Yu Liu^{1,3}, Milinda Abeykoon⁴, Eric D. Bauer³,
 Martin v. Zimmermann,² Weiguo Yin¹,,¹ Cedomir Petrovic¹, and Emil S. Bozin^{1,*}

¹*Condensed Matter Physics and Materials Science Division, Brookhaven National Laboratory, Upton, New York 11973, USA*

²*Deutsches Elektronen-Synchrotron DESY, Notkestrasse 85, Hamburg D-22607, Germany*

³*Los Alamos National Laboratory, Los Alamos, New Mexico 87545, USA*

⁴*Photon Sciences Division, Brookhaven National Laboratory, Upton, New York 11973, USA*



(Received 5 August 2022; revised 23 November 2022; accepted 29 November 2022; published 19 December 2022)

Superconductivity in binary ruthenium pnictides occurs proximal to and upon suppression of a nonmagnetic ground state, preceded by a pseudogap phase associated with Fermi surface instability, and its critical temperature, T_c , is maximized around the pseudogap quantum critical point. By analogy with isoelectronic iron-based counterparts, antiferromagnetic fluctuations became “usual suspects” as putative mediators of superconducting pairing. Here we report on a high-temperature local symmetry breaking in RuP, the nonsuperconducting parent of the maximum- T_c branch of these novel superconductors, revealed by combined nanostructure-sensitive powder and single-crystal x-ray total scattering analyses. Large local distortions of Ru chains associated with orbital-charge trimerization, further assembled into hexamers, exist above the two-stage electronic transition in RuP. In the pseudogap regime the precursors order with distortions retaining their strength, whereas they acquire spin-singlet characteristics which dramatically enhances the distortion as the nonmagnetic ground state establishes. The precursors enable the nonmagnetic ground state and presumed complex oligomerization, and the relevance of pseudogap fluctuations for superconductivity emerges as a distinct prospect. As a transition metal system in which partial d -manifold filling combined with high crystal symmetry promotes electronic instabilities, this represents a further example of local electronic precursors underpinning the macroscopic collective behavior of quantum materials.

DOI: [10.1103/PhysRevB.106.214516](https://doi.org/10.1103/PhysRevB.106.214516)

I. INTRODUCTION

Spatiotemporal fluctuations of electronic charge, orbital, and spin are native to the quantum materials realm [1–5], encompassing phenomena ranging from unconventional superconductivity (SC) [6,7], charge density waves [8,9], and pseudogaps (PGs) [10] to metal-insulator transitions [11,12], colossal magnetoresistivity [13], and frustrated magnetism [14,15]. Elucidating the character and role of electronic short-range correlations in the emergence of application-relevant phases [16–25] is challenging as most experimental probes yield bulk averages [26–28]. When the crystal lattice is involved, the pair distribution function (PDF) approach provides a unique perspective informing on the presence and nature of states of local broken symmetry on the nanoscale [29]. This is exemplified by the recent observation of structural fluctuations appearing alongside ferromagnetic order [30] greatly above the Verwey transition in magnetite (Fe_3O_4) [31], which illuminated a century old mystery of its mechanism [32] by revealing the essential role of magnetism in formation of the trimeron ground state [33]. Similarly, the discovery of structural fluctuations in iridium thiospinel (CuIr_2S_4) [34] unmasked an orbital precursor to its metal-insulator transition [35], amending the orbital-selective mechanism of the

octamer molecular orbital crystal state formation [36] proposed based on crystallography alone [37].

Metallic orthorhombic ($Pnma$) ruthenium pnictides RuPn ($Pn = \text{P, As, Sb}$), isoelectronic with FePn [38], display a complex electronic phase diagram derived from a nonmagnetic (NM) ground state [39–41] reached on cooling via a two-step symmetry breaking transition and intermediate PG phase [39,42,43]. Doping suppresses the NM state, leading to a dome-like SC in a narrow composition range around the PG phase quantum critical point (QCP), where superconducting T_c is maximized. This stereotypical landscape [44,45] suggests that fluctuations of some order parameter may aid superconductivity in RuPn . Antiferromagnetic fluctuations were indeed seen in the PG regime, but found to weaken appreciably on approaching the QCP [43,46]. Surprisingly, orbital and charge sectors [47] have not been considered in this context despite anomalous metallicity at high T , where a rather broad Drude-like component in optical conductivity was observed [40,48], indicative of strong carrier scattering.

Here we report on combined complementary x-ray total scattering based powder [49] and single-crystal [50] PDF analyses for nanoscale atomic structure determination utilized to explore orbital-charge fingerprints in RuP. This approach unveils local symmetry breaking Ru trimerization distortions in the high-temperature metallic state, above the two-stage electronic phase transition. Robust distortions, observed consistently in powder and crystal measurements, represent a

*bozin@bnl.gov

local response to the electronic structure instability imposed by global $Pnma$ symmetry. The instability, embodied in degenerate narrow flat Ru $4d_{xy}$ orbital-derived bands and corresponding partial density of states (DOS) sharply peaked at E_f [41,51], has thus far been assumed as the root cause of the two-stage global symmetry breaking transition [52]. The PDF analysis of RuP discovers that symmetry breaking associated with this instability in fact occurs already in the metallic regime, on ~ 15 Å length scale. This orbital-charge fluctuation, associated with the PG phase, acts as a precursor to the NM ground state and may be relevant for superconductivity in binary ruthenium pnictides. This observation further reinforces the notion of ubiquity of nanoscale precursors steering electronic properties in materials where partial d -manifold filling combined with high crystal symmetry promotes electronic instabilities.

The rest of the paper is organized as follows. In the next section a brief account of the measurements is provided. The physical properties, crystallographic transitions, and indicators of multiscale structure behavior are established in Sec. III A. Model-dependent assessment of the broken symmetry state and the local structure evolution with temperature from one-dimensional (1D) PDF are presented in Sec. III B. This is followed by model-independent characterization of local distortions in metallic regime using single-crystal diffuse scattering based three-dimensional (3D) differential PDF in Sec. III C. The origin of distortions, their character, and implications for the properties are discussed in Sec. IV A and Sec. IV B.

II. EXPERIMENTAL

RuP crystals were grown from excess Sn [53]. The magnetization was measured in a Quantum Design MPMS XL5. The powder total scattering experiment was carried out on cooling from 370 K to 10 K in 5 K steps at the 28-ID-1 beamline at the National Synchrotron Light Source II (NSLS II) at Brookhaven National Laboratory (BNL) in the rapid acquisition PDF mode [54], with an x-ray energy of 74.47 keV ($\lambda = 0.1665$ Å). Experimental PDFs were obtained following standard reduction protocols [55,56]. Structure analysis utilized well established small box modeling approaches [57–59]. Single-crystal total scattering data were collected at 350 K at the P21.1 beamline at the Positron Elektron Tandem Ring Anlage (PETRA III) facility at Deutsches Elektronen-Synchrotron (DESY), using an x-ray beam of 101.63 keV energy ($\lambda = 0.1220$ Å) sized to 0.5×0.5 mm². The 3D- Δ PDF analysis was carried out following procedures detailed in previous work [60]. Density functional theory (DFT) calculations were done by using the Vienna *Ab initio* Simulation Package [61–65]. Technical aspects of the methods are detailed in Supplementary Note 1 [66].

III. RESULTS

A. Average structure and properties

For $T > 330$ K RuP adopts the MnP-type $Pnma$ structure [39], featuring RuP₆ octahedra with face sharing along the a axis and edge sharing along the b axis and in the bc plane, Fig. 1(a), creating 3 nonequivalent Ru-Ru nearest-neighbor

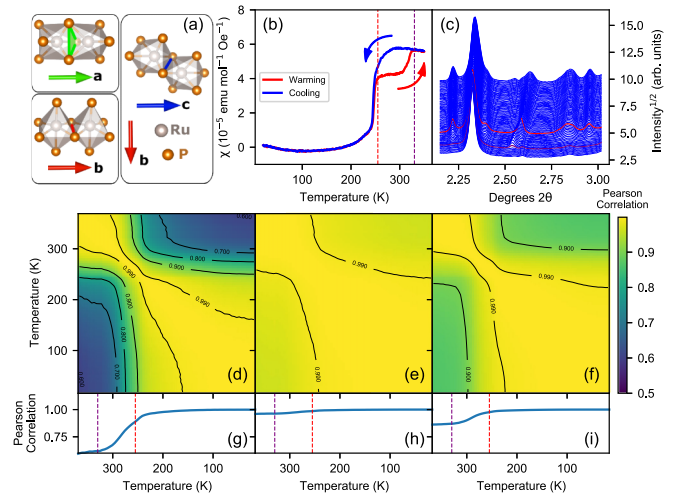


FIG. 1. RuP properties and transitions. (a) Three distinct types of RuP₆ octahedra connectivity: Face sharing along the a axis (green contacts), and edge sharing along the b and b/c axes (red and blue contacts, respectively). (b) Magnetic susceptibility (single crystal) on cooling and warming, depicting two transitions at $T_1 = 330$ K (purple dashed line) and $T_2 = 260$ K (red dashed line). (c) Temperature-dependent powder x-ray diffraction data (narrow 2θ range), with temperature decreasing from bottom to top, from 370 K to 10 K in 5 K steps. The diffraction patterns for $T_1 = 330$ K and $T_2 = 260$ K are shown in purple and red, respectively. Pearson correlation coefficient, computed between distinct temperature points comparing the PDF signal across (d), (g) 25–60 Å or (e), (h) 0–10 Å, as well as comparing (f), (i) the powder XRD signal across 1° – 15° 2θ . Panels (d), (e), (f) show the full Pearson correlation maps, while panels (g), (h), (i) present line cuts of these maps for $T = 10$ K, with T_1 and T_2 marked by purple and red dashed lines, respectively.

(NN) pairs. Shown in Figs. 2(a) and 2(b), the shortest contacts (green) constitute zigzag chains along the a axis, whereas the intermediate (blue) and long (red) contacts form zigzag ladders in the bc plane composed of straight rails (red) and zigzag rungs (blue).

Magnetic susceptibility, after subtraction of a low-temperature Curie tail, is consistent with a NM ground state showing two electronic phase transitions, Fig. 1, at $T_1 = 330$ K (from metal to PG phase) and $T_2 = 260$ K (from PG to NM phase) consistent with previous reports [39,40]. Total scattering powder diffraction data disclose two global symmetry breaking structural transitions. Formation of new, weak, Bragg peaks at T_1 [Fig. 1(c), purple trace], specifically at about 2.20° and 2.55° 2θ , indicates an onset of ordering below the PG transition. Further changes in the diffraction profile around T_2 [Fig. 1(c), red trace] evidence transition to the NM ground state. The 370 K Bragg data are consistent with the $Pnma$ symmetry (Rietveld fit; Supplementary Note 2 [66]). However, the model yields rather large U_{22} atomic displacement parameter (ADP) of Ru [$0.0168(5)$ Å²] as compared to U_{11} [$0.0042(5)$ Å²] and U_{33} [$0.0054(3)$ Å²]. This additional high-temperature anomaly points to structural disorder along the b axis.

The Pearson correlation coefficient (defined in Supplementary Note 1 [66]) calculated for temperature-dependent powder PDF data over an r range which includes only the

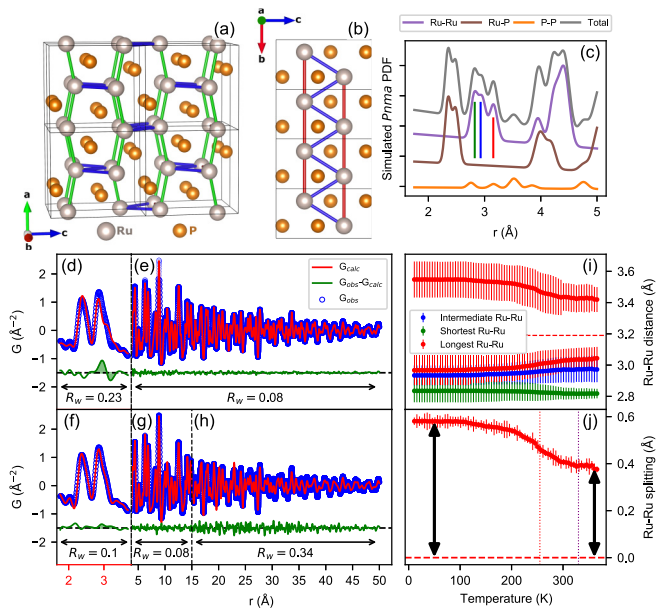


FIG. 2. Local structure from powder PDF. Eight unit cells of the $Pnma$ structure of RuP viewed along the (a) b axis and (b) a axis. Three distinct Ru-Ru nearest-neighbor pairs are shown as solid lines: green, blue, and red contacts correspond to the shortest, intermediate, and longest pair distances, respectively. (c) A simulated RuP x-ray PDF, decomposed into the partial pair contributions. The PDF contributions from the three $Pnma$ symmetry-allowed Ru-Ru nearest-neighbor pairs shown in (a) and (b) are identified by identically colored vertical lines. PDF fit of the experimental PDF signal measured at 370 K utilizing the $Pnma$ model shows (d) a large misfit at about 3.1 Å, the approximate location of Ru-Ru pairs. The fit quality over this range is poor, resulting in $R_w = 23\%$. Over (e) a broader r range, the $Pnma$ model fit is adequate, with $R_w = 8\%$. PDF fit of the 370 K data utilizing the $P2_1/c$ constrained model (f) remedies the misfit at about 3.1 Å, resulting in $R_w = 10\%$. The fit is adequate (g) up to about 15 Å, with $R_w = 8\%$, but (h) extending the calculation range reveals inadequacy of local structure model in describing the longer-range structure ($R_w = 34\%$). (i) Ru-Ru pair distance vs temperature, extracted from the $P2_1/c$ fit up to 15 Å, reveals the primary symmetry breaking on the longest Ru-Ru pairs, parallel to the $Pnma$ b axis. (j) The magnitude of the Ru-Ru distance splitting along the $Pnma$ b axis.

long-range structure and excludes the local structure [15 < r < 60 Å; Figs. 1(d) and 1(g)], shows two distinct regions of self-similarity, with a single region of strong dissimilarity bounded by $T = 260$ K, demonstrating that a long-range structural phase transition at T_2 is apparent here. Conversely, when considering an r range which includes only the local structure [$0 < r < 15$ Å; Figs. 1(e) and 1(h)], the region of dissimilarity at $T = 260$ K is considerably less pronounced, with no discernible change at T_1 . The Pearson correlation coefficient of the total scattering signal [Figs. 1(f) and 1(i)], which represents the effects of both the long-range and local structure, again shows a single region of dissimilarity bounded by $T = 260$ K. This dissimilarity is weaker than that observed when considering the long-range PDF [Figs. 1(d), 1(g)] but stronger than that observed when considering the local structure PDF [Figs. 1(e) and 1(h)]. This correlation analy-

sis establishes distinct structural manifestations on different length scales.

B. Local structure from powder PDF

To characterize structural disorder above the PG phase ($T > T_1$) and its temperature evolution, we use powder PDF analysis. A fit of the $Pnma$ model to 370 K data over $1.75 < r < 50$ Å is shown in Figs. 2(d) and 2(e). While the model adequately reproduces the observed PDF for $r > 3.9$ Å, it fails for $r < 3.9$ Å. A large misfit around 3.1 Å, highlighted on the residual curve in Fig. 2(d), reveals a short-range distortion incompatible with average symmetry. The $Pnma$ model, which is consistent with the majority of the observed PDF signal, dictates that atom pairs (PDF intensity) should be present at a larger r than is seen in the experimental data; the observed intensity is transferred to lower r compared to the model.

Inspection of a simulated PDF, decomposed into atom-pair specific partial contributions, Fig. 2(c), discloses that the intensity in this region predominately originates from 3 distinct Ru-Ru NN contributions in the $Pnma$ structure described above. The high- r portion of this 3.1 Å feature comes from the longest of these Ru-Ru NN pairs, which form the rails of the zigzag ladder along the b axis and have edge-sharing RuP₆ connectivity, marked in red in Figs. 1(a) and 2(b).

The local distortion was assessed with a model utilizing monoclinic $P2_1/c$ constraints [41] (relationship to $Pnma$ is detailed in Supplementary Note 3 [66]). Fit of this broken symmetry model to the PDF data at 370 K over the range $1.75 < r < 15$ Å, shown in Figs. 2(f) and 2(g), explains the PDF data well, and remedies the $Pnma$ model misfit at 3.1 Å. While the $P2_1/c$ model describes the local structure well, it poorly fits the data at higher r ; if this model is used to compute the predicted PDF signal for $r > 15$ Å, there is significant disagreement between the model and observed PDF at 370 K, Fig. 2(h). The measured signal in the high- r region is visibly sharper than the $P2_1/c$ model signal, consistent with higher ($Pnma$) symmetry on longer length scales in this temperature regime.

The temperature evolution of the local structure was quantified by fitting the PDF data for $10 < T < 370$ K with the $P2_1/c$ model for $1.75 < r < 15$ Å. We have then assigned each of the pairs in the refined $P2_1/c$ cell to the associated pair present in the $Pnma$ cell. This assignment should yield 3 unique groups, each composed of 36 Ru-Ru NN pairs [41]. We however found that the group associated with Ru-Ru NN pairs parallel to the $Pnma$ b axis [red connections in Fig. 1(a) and Figs. 2(a) and 2(b)] was bimodal, with 24 Ru-Ru NN pairs showing a shorter mean pair distance and 12 pairs showing a longer mean distance, that is, a ratio of 2:1 of short:long pairs.

The pair distance distribution extracted from the $P2_1/c$ model fits is presented in Fig. 2(i). Here, the circles represent the mean of the Ru-Ru pair distance population, whereas the vertical bars represent the standard deviation of this population. The colors are consistent with the Ru-Ru pairs shown in Fig. 1(a) and Figs. 2(a)–2(c), where the pairs forming rails along the b axis, red markers in Fig. 2(i), are split into two subpopulations. At 370 K the splitting, Fig. 2(i), is ≈ 0.4 Å, a remarkably large distortion by crystallographic standards. The magnitude does not change upon entering the PG phase,

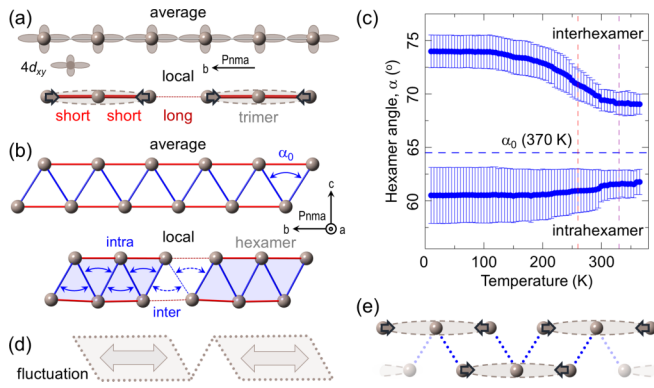


FIG. 3. Local distortions at 370 K. (a) Homogeneous chains with $4d_{xy} t_{2g}$ Ru orbitals ($Pnma$ average view, top) undergo trimerization distortions ($P2_1/c$ local view, bottom). (b) Regular zigzag ladders in the bc plane ($Pnma$ average view, top) break into hexamer segments ($P2_1/c$ local view, bottom). (c) Local hexamer bond angle, $\alpha(T)$: symbols represent mean values; vertical bars are standard deviations. Uniform average (α_0 , horizontal dashed line, $Pnma$ view), and local bimodal distribution of intrahexamer ($\alpha < \alpha_0$) and interhexamer ($\alpha > \alpha_0$) angles (2:1 relative abundance, $P2_1/c$ view). (d) Orientational hexamer fluctuation. (e) Nonhexamer configuration of trimers on a zigzag ladder.

but increases substantially in the NM phase, reaching 0.6 \AA at 100 K.

The undistorted global $Pnma$ structure in the metallic regime hosts a complex local distortion, revealed by interatomic distances and angles derived from a $P2_1/c$ model fit. Crystallographically, the zigzag ladders in the bc planes are undistorted, featuring uniform distances along the b axis and bridging rung contacts [Fig. 3(a), top], with identical rung bond angles, α_0 [Fig. 3(b), top]. Locally, the structure exhibits a short-short-long sequence of Ru-Ru distances along the b axis [Fig. 3(a), bottom]. This portrays nearly linear Ru trimers, a consequence of bond-charge disproportionation, suggesting residual covalency and charge localization above T_1 . Additionally, the rung bond angles from local $P2_1/c$ model form a nonuniform bimodal distribution: 4 adjacent angles are observably smaller than the crystallographic average, $\alpha < \alpha_0$, whereas 2 adjacent angles are significantly larger, $\alpha > \alpha_0$ [Fig. 3(b), bottom, and Fig. 3(c)]. This implies that local Ru trimers arrange into hexamers on the zigzag ladder. In contrast, the Ru distances constituting uniform zigzag chains along the $Pnma$ a axis have a rather narrow local distribution ($0.04\text{--}0.08 \text{ \AA}$), Fig. 2(i), as they do not distort appreciably at high temperature. The dominant distortion at $T > T_1$ originates from Ru trimers aligned into hexamers. There is no discernible out of plane coupling, consistent with a quasi-one-dimensional disorder implicated by the ADP anisotropy.

The magnitude of local distortions changes marginally on cooling across T_1 , whereas its *dramatic increase* is observed below T_2 , as shown in Figs. 2(i) and 2(j), and Fig. 3(c).

C. Local structure from single crystal PDF

The observations garnered from the powder PDF analysis establish the presence of a local structure distortion and provide insights into its nature. A complementary view of

the distortion, independent of $P2_1/c$ model, is offered by a 3D- Δ PDF analysis [50] that probes the difference between the average and local structures directly [67]. This enables exploring the distortions in the metallic phase (at 350 K) in RuP crystal specimen, and their 3D aspects.

The diffuse intensity distribution shows broad, rodlike signal in the $Q_z = 0 \text{ \AA}^{-1}$ slice, running parallel to the Q_y direction, as shown in Fig. 4(a). The diffuse intensity is not confined to planes containing Bragg peaks, and also shows interesting features between Bragg peaks, as can be seen in Fig. 4(b), implying short-range correlations.

The corresponding 3D- Δ PDF is highly anisotropic (Supplementary Note 4 [66]), with the strongest features found in the $Z = 0 \text{ \AA}$ plane, confined to line $X = 0 \text{ \AA}$, as highlighted in Figs. 4(c)–4(e). These features are coincident with the location of overlapping Ru-Ru and P-P pair vectors. However, the dominant contribution is from Ru-Ru rather than P-P pairs, as the former have an order of magnitude stronger scattering scale [see Fig. 2(c)], and inspection of \mathbf{r} locations where nonoverlapping P-P pair correlation vectors are expected shows rather weak signal. The locations of the strongest observed features are exactly those implicated in the powder PDF analysis, representing Ru-Ru pairs running parallel to the orthorhombic b axis. As highlighted in Figs. 4(f) and 4(g), 3D- Δ PDF correlations are weak in the $Z = 0 \text{ \AA}$ plane along the X direction and are of the opposite sign (blue-red-blue, corresponding to negative-positive-negative) to those observed along the Y direction (red-blue-red), corresponding to in-phase correlated thermal vibrations with no observable displacive component [50].

The signal associated with Ru-Ru correlations in the $Z = 0 \text{ \AA}$ plane along the line $X = 0 \text{ \AA}$ is rather unique. The first feature at $Y = 3.1 \text{ \AA}$ contains a central negative (blue) lobe, with two outer positive (red) lobes [see, e.g., Fig. 4(h)], indicating that Ru-Ru nearest neighbors, marked by red bonds throughout this work, are displaced off the average pair position, along the orthorhombic b axis. This is consistent with bimodal distribution of Ru-Ru interatomic vectors in this direction. Importantly, the positive lobe closer to the origin is about twice as strong as the positive lobe farther from the origin, suggesting that Ru-Ru nearest neighbors in the local structure adopt a 2:1 ratio of short to long bonds along the orthorhombic b axis, indicative of a Ru trimer and consistent with powder PDF observations.

The 3D- Δ PDF also provides insights on rail-to-rail correlations within the zigzag ladder in the orthorhombic bc plane. The $Z = 2.5 \text{ \AA}$ plane along the line $X = 0 \text{ \AA}$ shown in Fig. 5(c) gives information on neighboring Ru chains along the orthorhombic c axis, as shown in Fig. 5(a). The NN Ru-Ru pairs along this direction, highlighted in Fig. 5(a) by blue connections, do not show a distortion off the average structure site, but show a positive Δ PDF lobe at the location of the average structure NN Ru-Ru pair, the signature of strong bonding. Conversely, Ru-Ru next-NN pairs along this direction, highlighted in Fig. 5(a) by purple connections, do exhibit a displacive distortion off the average structure site. This indicates existence of shorter and longer next-NN inter-rail pairs and supports the powder PDF observation of a hexamer-like association of local trimers on the ladder.

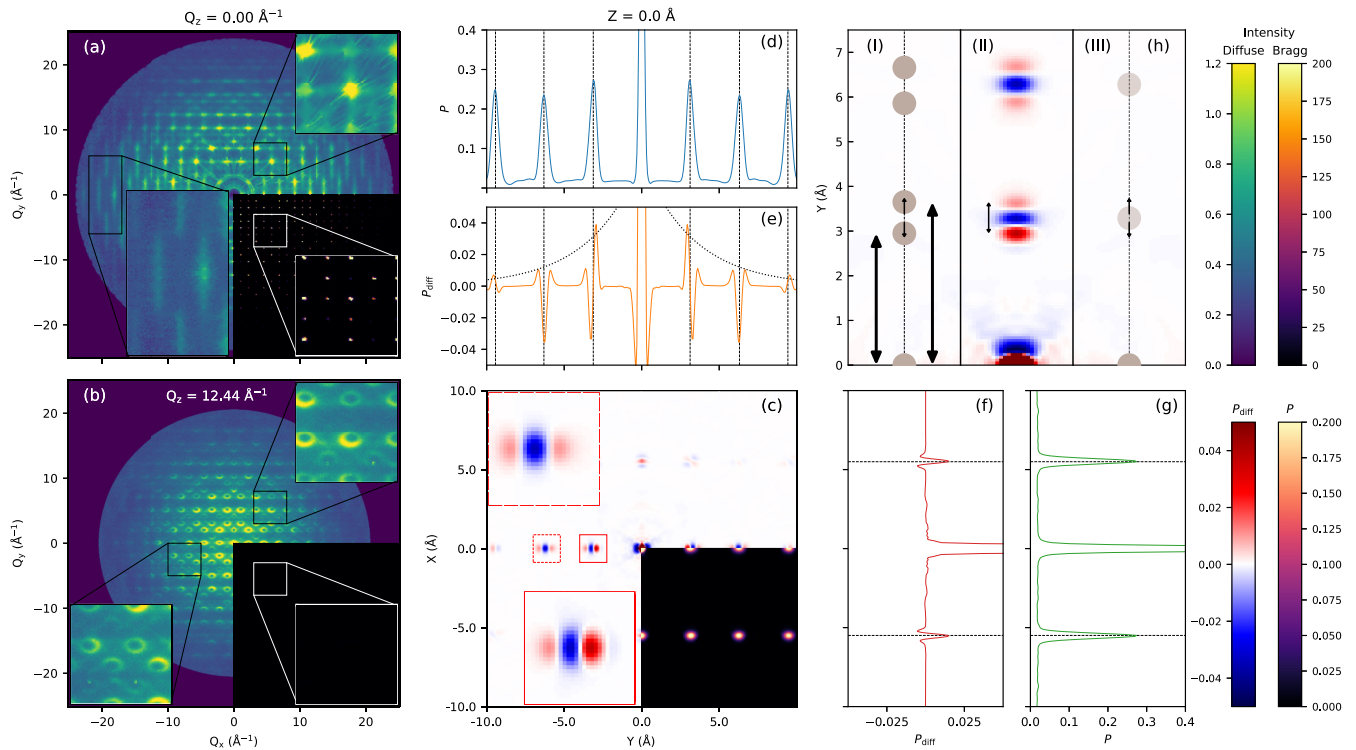


FIG. 4. Single-crystal view of the local state at high temperature. Slices of the diffuse intensity distribution measured from a RuP single crystal at 350 K at (a) $Q_z = 0.00 \text{ \AA}^{-1}$ (containing Bragg peaks) and at (b) $Q_z = 12.44 \text{ \AA}^{-1}$ (between Bragg peaks). The lower right quadrants in (a) and (b) contain the full intensity distribution and are shown over a broad intensity range to highlight Bragg peaks, while other quadrants are a result of removing all Bragg peaks and shown over a narrower intensity range. Features of interest are shown inset on an enlarged scale. After Fourier transform, the (c) $Z = 0 \text{ \AA}$ cut of the 3D- Δ PDF shows the most significant features. The full 3D-PDF is shown in the lower right quadrant of (c) to illustrate the average position of the Ru-Ru pairs in this plane, with the Ru-Ru nearest-neighbor and next-nearest-neighbor features shown enlarged in the lower and upper left insets, respectively. Line cuts for the Δ and full PDF at $Z = 0 \text{ \AA}$ along the [(d) and (e), respectively] Y and [(f) and (g), respectively] X axes are shown, with the position of Ru-Ru pairs highlighted by dotted black lines. Dotted envelope in (e) illustrates a decay of local correlations. The 3D- Δ PDF signal along the $X = Z = 0 \text{ \AA}$ is consistent with the presence of trimers along this direction, as depicted in (h). Strong (blue) negative features in (hIII) indicate that Ru-Ru pairs in the local structure are displaced off the average pair distance, shown along the dashed line and shifted to the right for clarity (hIII). Strong (red) positive features in (hII) indicate these Ru-Ru pairs are shifted to longer and shorter distances in the local structure, as represented by gray circles and marked by black arrows along the left-shifted dashed line (hI). The local distortion moving Ru-Ru nearest-neighbor pairs to shorter r is about twice as likely as that moving these pairs to greater r , as implied by relative intensity of the features, consistent with the presence of two short and one long bond associated with trimerization.

The $Z = 0.5 \text{ \AA}$ plane, shown in Fig. 5(d), gives information on Ru-Ru correlations in the orthorhombic ab plane, as shown in Fig. 5(b). The NN Ru-Ru pairs in this plane, highlighted in Fig. 5(b) by green connections, do not show a dispersive distortion off the average structure site, but show a positive Δ PDF lobe at the location of the average structure NN Ru-Ru pair, reflecting in-phase thermal motion, associated with strong bonding. Similarly, Ru-Ru next-NN pairs in this plane, highlighted in Fig. 5(b) by orange connections, also do not show a dispersive distortion off the average structure site. This, taken together with the $P2_1/c$ model derived powder PDF observations of rather small distortions of the green zigzag chains along the orthorhombic a axis, suggests weak interladder hexamer correlations.

Deviations from the average $Pnma$ structure are not detected beyond 15 \AA in powder PDF analysis, whereas the signatures of dispersive distortions in 3D- Δ PDF are highly anisotropic and confined to the orthorhombic bc plane over a similarly narrow spatial range. This corroborates

quasi-one-dimensional character of fluctuations correlated over a length scale of about two hexamer units.

IV. DISCUSSION AND CONCLUSIONS

A. Ru₆ hexamers: Origin and fluctuations

The driving force behind this peculiar local oligomer/hexamer built of trimers at high temperature is the Fermi surface instability imposed by $Pnma$ symmetry and nominal $4d^5$ filling, embodied in flat degenerate bands of Ru $4d_{xy} t_{2g}$ orbital character and DOS peaked at E_f [41,51,52]. Observed sizable bifurcation distortions result from simultaneous contraction of adjacent Ru pair distances sharing central Ru. Due to edge-sharing RuP₆ connectivity along the b axis, Fig. 1(a), the distortions involve precisely $t_{2g} xy$ orbital overlaps, Fig. 3(a). Large distortions of the longest of the three distinct NN Ru pair distances necessitate bond-charge disproportionation and increased covalency of the short Ru-Ru contacts, pointing to their electronic origin.

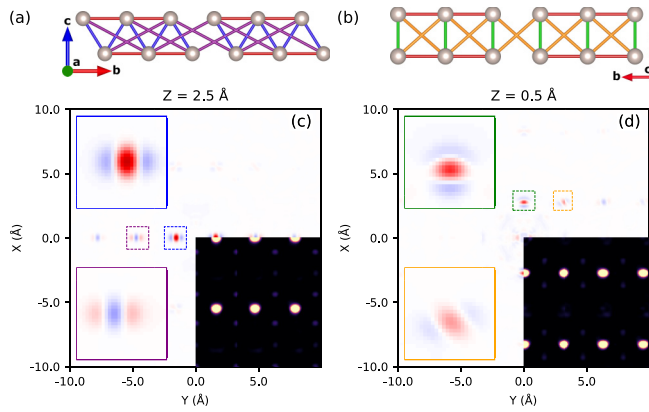


FIG. 5. Local Ru inter-rail correlations. Diagrams depicting Ru chains running along the $Pnma$ b axis as viewed along the (a) $Pnma$ a axis and (b) $Pnma$ c axis. The relevant 3D- Δ PDF slices at $Z = 2.5$ Å and $Z = 0.5$ Å are shown in (c) and (d), respectively. The 3D- Δ PDF feature associated with Ru-Ru NN pairs connected by blue lines in (a) is highlighted in the blue square in (c), while that associated with Ru-Ru next-NN pairs connected by purple lines in (a) is highlighted in the purple square in (c). Similarly, Ru-Ru NN and next-NN pairs are marked by green and orange contacts, respectively, in (b) and highlighted in squares of matching color in (d). Total 3D-PDF, shown in the lower right quadrant of (c) and (d), illustrates the average location of the Ru-Ru pair vectors in these planes.

This picture is further supported by DFT calculations on fully converged average and local models of the 370 K PDF data. Calculations using the orthorhombic average structure reproduce the instability; flat bands are seen in the T - R (along the $Pnma$ a axis) and R - S (along the $Pnma$ c axis; Supplementary Note 5 [66]) directions, Fig. 6(b), with peak in DOS at E_f , black trace in Fig. 6(a). In contrast, calculations using global monoclinic distorted phase based on the local model show removal of the instability, Fig. 6(c), by opening a small gap around the T - R - S line and splitting of DOS at E_f [red trace in Fig. 6(a)] thus lifting the degeneracy of the flat bands, albeit partially. While further theoretical investigations are necessary to fully comprehend the exact mechanism behind the monoclinic distortion and metal to insulator transition, our calculations confirm causality between the electronic instability and crystallographic symmetry breaking. The distortions driven by this instability could then be considered as a fingerprint of PG fluctuations. This is further corroborated by the fact that local distortions retain their magnitude and character upon entering the PG phase, Figs. 2(i) and 2(j) and Fig. 3(c). It is this nanoscale temperature invariance of the distortions that qualifies them as fluctuations of the PG phase.

In this picture the trimerization represents a primary response, with the hexamers being, arguably, a consequence of elastic energy penalty minimization associated with short-range trimer correlations. To illustrate this, we consider a nonhexamer arrangement of trimers on a ladder, Fig. 3(e), where the trimers on the opposite rails are offset by one Ru position with respect to their hexamer arrangement depicted in Fig. 3(b). Here, the central Ru atom of the trimer on the bottom rail faces the long intertrimer distance on

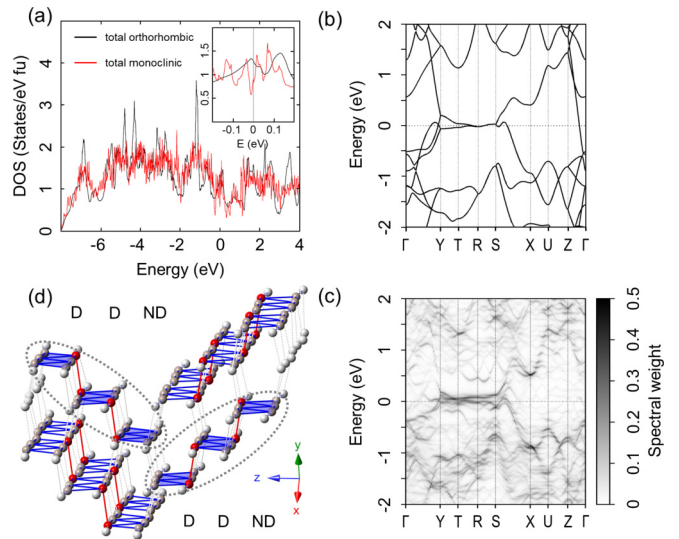


FIG. 6. Electronic structure and Ru oligomerization. (a) Comparison of DOS calculated for the orthorhombic and monoclinic structures derived from 370 K PDF analysis. Inset: DOS near E_f reveals ~ 100 meV splitting. Unfolded band structure in the Brillouin zone of the orthorhombic cell for (b) undistorted orthorhombic structure expressed in the monoclinic setting and (c) distorted monoclinic structure, where the line intensity reflects spectral weight. In (c), a small gap opens along the direction of the flat bands (T - R - S), consistent with the splitting of DOS in (a). (d) Segment of distorted structure from 15 Å fit to 10 K PDF data. The zigzag chains, undistorted in the orthorhombic structure, form triplets composed of two chain types. The first type, D, features shorter (~ 2.79 Å) dimer-like Ru-Ru contacts (colored red) connecting three Ru_6 hexamers on adjacent ladders, and longer Ru-Ru contact (~ 2.85 Å on average). The second type, ND, is less distorted and with no dimer-like contacts. The triplet consists of two D-type chains and one ND-type chain. Hexamers organize into higher-order oligomers, implying modified orbital occupancy at T_2 as interladder correlations develop.

the top rail. Compared to the hexamer configuration, this configuration involves a larger number of energetically expensive rung bond-stretching distortions, dotted blue lines in Fig. 3(e). Since the trimer pairing minimizes bond stretching and engages fewer energetically less expensive bond-bending distortion modes, hexamer formation is likely favored.

The undistorted structure is retrieved by spatiotemporal averaging of the distortions. As an energy-integrating method, PDF does not distinguish static from dynamic distortions. While purely static distortions, incoherently distributed across the ladders and randomized by defects, would be consistent with lack of long-range order, local distortions are more likely dynamic, brought about by temporal fluctuations of the trimer bond/charge. Dynamic alternations of hexamer orientations, illustrated in Fig. 3(d), are expected to be entropically stabilized.

B. Implications for electronic properties

The observed Ru_6 fluctuations provide a rationale for poor metallic conduction of RuP above the two-stage transition, seen previously in some metallic spinels [34,68]. They further act as a precursor to the two-stage transition, evident from the

evolution of local distortion with temperature, Fig. 2(i) and Fig. 3(c).

The lack of local structure changes at T_1 implies the PG transition has an *order-disorder* character (see Supplementary Note 6 [66]), where hexamer stripes are gradually formed, governed by an energy scale lower than that of hexamer formation. This is consistent with reported temperature dependence of the Knight shifts across the metal-PG transition in RuP [43]. Interhexamer correlations grow in the PG phase on approaching the NM transition, coincident with antiferromagnetic fluctuations seen by nuclear magnetic resonance [43,46]. The intrahexamer bonding strengthens, reflected in contraction of blue (rungs) and short red (intratrimer) Ru-Ru distances, Fig. 2(i), whereas the intraladder interhexamer coupling weakens, seen as relaxation of intertrimer contacts [long red distances in Fig. 2(i)] and interhexamer angles [top branch in Fig. 3(c)]. Notably, the distribution of Ru-Ru contacts along the orthorhombic a axis [zigzag chains; green data in Fig. 2(i)] broadens, implying development of 3D interhexamer correlations.

Below T_2 , in the NM phase, the local structure changes more abruptly, and the bimodal splitting, Fig. 2(j), increases by 50% as hexamers compact and distance from each other on the ladders. Such large local distortion enhancements were found in systems with spin-singlet ground states exhibiting orbital molecules [34,68,69]. Interestingly, fits of $Pnma$ and $P2_1/c$ models to the diffraction data, although both strictly inadequate, indicate negative thermal expansion of respective (a, b) and (a, c) axes in the PG phase (Supplementary Note 3 [66]). Similar negative thermal expansion was seen in CrSe₂ [70] in association with metal cluster fluctuations, where Peierls-like instability leads to an orbitally ordered ground state of linear trimers [71]. While detailed crystallographic characterization is required to grasp the full complexity of the ground state, assessment of local structure from 10 K PDF fit suggests further complex oligomerization such as depicted in Fig. 6(d). The structure features two types of zigzag chains consistent with cell tripling in all three directions (see Supplementary Note 7 [66]). Two neighboring chains of one type [D in Fig. 6(d)] are distorted and carry short dimer-like interhexamer contacts, whereas the third chain constituting the other type [ND in Fig. 6(d)] does not exhibit such short contacts. This results in triplets of dimer-bound hexamers. We recently became aware of a report of the ground state structure of RuP, confirming the $P2_1/c$ symmetry and linear Ru trimerization involving orbital molecules proposed to be associated with four electron/three center bonding [72]. This is consistent with the low-temperature local structure retrieved from the 1D-PDF analysis. We note that the trimers in the NM

phase are likely electronically distinct from those observed in the PG and metallic regimes. This invites a detailed local spectroscopic survey of the Ru valence state evolution across different electronic phases.

In summary, orbital-charge fluctuations of the PG phase, fingerprints of which are established here, are an important hitherto overlooked ingredient of the complex phase diagram of binary RuPn. The electron-doping induced SC state in both RuP and RuAs derived compositions with a maximum transition temperature, at the QCP of the PG phase, was attributed to the conventional single-band weak coupling Bardeen-Cooper-Schrieffer (BCS) model [73]. Notably, a linear temperature dependence of the upper critical field, H_{c2} , persists down to the lowest temperature with no saturation tendency, a behavior not expected for an isotropic single-band BCS superconductor. This observation, as well as dramatically different SC dome maximum transition temperatures in RuP, RuAs, and RuSb families [39], raises an important question, in light of our PDF observations, of the exact role of orbital-charge fluctuations in SC pairing [74] and/or enhancement of T_c , e.g., via tuning of the effective electron-hole interactions [44], near the PG quantum critical point [75] as well as of the interplay with reported antiferromagnetic fluctuations in the PG regime. Systematic mapping of orbital-charge fluctuations across the complex electronic phase diagram of binary RuPn would be highly desirable to address this matter.

ACKNOWLEDGMENTS

We gratefully acknowledge Olof G. for assistance with the single-crystal measurements, and J. D. Thompson for collecting the magnetic susceptibility data. Work at Brookhaven National Laboratory was supported by the U.S. Department of Energy, Office of Science, Office of Basic Energy Sciences (DOE-BES), under Contract No. DE-SC0012704. We acknowledge DESY (Hamburg, Germany), a member of the Helmholtz Association HGF, for the provision of experimental facilities. Parts of this research were carried out at beamline P21.1 at PETRA III. E.S.B. acknowledges the Stephenson Distinguished Visitor Programme for supporting his stay at DESY in Hamburg. This research was supported in part through the Maxwell computational resources operated at Deutsches Elektronen-Synchrotron DESY, Hamburg, Germany. Work at Los Alamos National Laboratory was performed under the auspices of the U.S. Department of Energy, Office of Basic Energy Sciences, and Division of Materials Sciences and Engineering under the project ‘‘Quantum Fluctuations in Narrow Band Systems.’’

[1] B. Keimer and J. E. Moore, *Nat. Phys.* **13**, 1045 (2017).

[2] S. T. Bramwell, K. Christensen, J.-Y. Fortin, P. C. W. Holdsworth, H. J. Jensen, S. Lise, J. M. López, M. Nicodemi, J.-F. Pinton, and M. Sellitto, *Phys. Rev. Lett.* **84**, 3744 (2000).

[3] L. A. Boyarskii, S. P. Gabuda, and S. G. Kozlova, *Low Temp. Phys.* **31**, 308 (2005).

[4] R. M. Fernandes, P. P. Orth, and J. Schmalian, *Annu. Rev. Condens. Matter Phys.* **10**, 133 (2019).

[5] S. Paschen and Q. Si, *Nat. Rev. Phys.* **3**, 9 (2021).

[6] N. Auvray, B. Loret, S. Benhabib, M. Cazayous, R. D. Zhong, J. Schneeloch, G. D. Gu, A. Forget, D. Colson, I. Paul *et al.*, *Nat. Commun.* **10**, 5209 (2019).

[7] T. Chen, Y. Chen, A. Kreisel, X. Lu, A. Schneidewind, Y. Qiu, J. T. Park, T. G. Perring, J. R. Stewart, H. Cao *et al.*, *Nat. Mater.* **18**, 709 (2019).

- [8] D. H. Torchinsky, F. Mahmood, A. T. Bollinger, I. Bozovic, and N. Gedik, *Nat. Mater.* **12**, 387 (2013).
- [9] Y. I. Joe, X. M. Chen, P. Ghaemi, K. D. Finkelstein, G. A. de la Peña, Y. Gan, J. C. T. Lee, S. Yuan, J. Geck, G. J. MacDougall *et al.*, *Nat. Phys.* **10**, 421 (2014).
- [10] M. J. Rice and S. Strässler, *Solid State Commun.* **13**, 1389 (1973).
- [11] S. Hoshino and P. Werner, *Phys. Rev. Lett.* **118**, 177002 (2017).
- [12] Y. Feng, Y. Wang, D. M. Silevitch, S. E. Cooper, D. Mandrus, P. A. Lee, and T. F. Rosenbaum, *Nat. Commun.* **12**, 2779 (2021).
- [13] V. B. Shenoy, T. Gupta, H. R. Krishnamurthy, and T. V. Ramakrishnan, *Phys. Rev. Lett.* **98**, 097201 (2007).
- [14] C. Stock, L. C. Chapon, O. Adamopoulos, A. Lappas, M. Giot, J. W. Taylor, M. A. Green, C. M. Brown, and P. G. Radaelli, *Phys. Rev. Lett.* **103**, 077202 (2009).
- [15] B. Freelon, R. Sarkar, S. Kamusella, F. Brückner, V. Grinenko, S. Acharya, M. Laad, L. Craco, Z. Yamani, R. Flacau *et al.*, *npj Quantum Mater.* **6**, 4 (2021).
- [16] S. Watanabe and K. Miyake, *J. Phys. Soc. Jpn.* **71**, 2489 (2002).
- [17] T. Yokoya, T. Kiss, A. Chainani, S. Shin, and K. Yamaya, *Phys. Rev. B* **71**, 140504(R) (2005).
- [18] A. J. Drew, F. L. Pratt, T. Lancaster, S. J. Blundell, P. J. Baker, R. H. Liu, G. Wu, X. H. Chen, I. Watanabe, V. K. Malik *et al.*, *Phys. Rev. Lett.* **101**, 097010 (2008).
- [19] J. K. Glasbrenner, I. I. Mazin, H. O. Jeschke, P. J. Hirschfeld, R. M. Fernandes, and R. Valenti, *Nat. Phys.* **11**, 953 (2015).
- [20] S. Lederer, Y. Schattner, E. Berg, and S. A. Kivelson, *Phys. Rev. Lett.* **114**, 097001 (2015).
- [21] B. A. Frandsen, K. M. Taddei, M. Yi, A. Frano, Z. Guguchia, R. Yu, Q. Si, D. E. Bugaris, R. Stadel, R. Osborn *et al.*, *Phys. Rev. Lett.* **119**, 187001 (2017).
- [22] B. Loret, N. Auvray, Y. Gallais, M. Cazayous, A. Forget, D. Colson, M.-H. Julien, I. Paul, M. Civelli, and A. Sacuto, *Nat. Phys.* **15**, 771 (2019).
- [23] R. Arpaia, S. Caprara, R. Fumagalli, G. D. Vecchi, Y. Y. Peng, E. Andersson, D. Betto, G. M. D. Luca, N. B. Brookes, F. Lombardi *et al.*, *Science* **365**, 906 (2019).
- [24] L. Poudel, J. M. Lawrence, L. S. Wu, G. Ehlers, Y. Qiu, A. F. May, F. Ronning, M. D. Lumsden, D. Mandrus, and A. D. Christianson, *npj Quantum Mater.* **4**, 52 (2019).
- [25] S. Wu, Y. Song, Y. He, A. Frano, M. Yi, X. Chen, H. Uchiyama, A. Alatas, A. H. Said, L. Wang *et al.*, *Phys. Rev. Lett.* **126**, 107001 (2021).
- [26] S. Hoshino and P. Werner, *Phys. Rev. Lett.* **115**, 247001 (2015).
- [27] M. S. Ikeda, T. Worasaran, E. W. Rosenberg, J. C. Palmstrom, S. A. Kivelson, and I. R. Fisher, *Proc. Natl. Acad. Sci. USA* **118**, e2105911118 (2021).
- [28] T. Schäfer and A. Toschi, *J. Phys.: Condens. Matter* **33**, 214001 (2021).
- [29] S. J. L. Billinge and I. Levin, *Science* **316**, 561 (2007).
- [30] G. Perversi, E. Pachoud, J. Cumby, J. M. Hudspeth, J. P. Wright, S. A. J. Kimber, and J. P. Attfield, *Nat. Commun.* **10**, 2857 (2019).
- [31] E. J. W. Verwey, *Nature (London)* **144**, 327 (1939).
- [32] F. Walz, *J. Phys.: Condens. Matter* **14**, R285(R) (2002).
- [33] M. S. Senn, J. P. Wright, and J. P. Attfield, *Nature (London)* **481**, 173 (2012).
- [34] E. S. Bozin, W. G. Yin, R. J. Koch, M. Abeykoon, Y. S. Hor, H. Zheng, H. C. Lei, C. Petrovic, J. F. Mitchell, and S. J. L. Billinge, *Nat. Commun.* **10**, 3638 (2019).
- [35] T. Furubayashi, T. Matsumoto, T. Hagino, and S. Nagata, *J. Phys. Soc. Jpn.* **63**, 3333 (1994).
- [36] P. G. Radaelli, Y. Horibe, M. J. Gutmann, H. Ishibashi, C. H. Chen, R. M. Ibberson, Y. Koyama, Y. S. Hor, V. Kiryukhin, and S. W. Cheong, *Nature (London)* **416**, 155 (2002).
- [37] D. I. Khomskii and T. Mizokawa, *Phys. Rev. Lett.* **94**, 156402 (2005).
- [38] Q. Si, R. Yu, and E. Abrahams, *Nat. Rev. Mater.* **1**, 16017 (2016).
- [39] D. Hirai, T. Takayama, D. Hashizume, and H. Takagi, *Phys. Rev. B* **85**, 140509(R) (2012).
- [40] R. Y. Chen, Y. G. Shi, P. Zheng, L. Wang, T. Dong, and N. L. Wang, *Phys. Rev. B* **91**, 125101 (2015).
- [41] H. Kotegawa, K. Takeda, Y. Kuwata, J. Hayashi, H. Tou, H. Sugawara, T. Sakurai, H. Ohta, and H. Harima, *Phys. Rev. Mater.* **2**, 055001 (2018).
- [42] K. Sato, D. Ootsuki, Y. Wakisaka, N. L. Saini, T. Mizokawa, M. Arita, H. Anzai, H. Namatame, M. Taniguchi, D. Hirai *et al.*, [arXiv:1205.2669](https://arxiv.org/abs/1205.2669).
- [43] S. Li, Y. Kobayashi, M. Itoh, D. Hirai, and H. Takagi, *Phys. Rev. B* **95**, 155137 (2017).
- [44] D. N. Basov and A. V. Chubukov, *Nat. Phys.* **7**, 272 (2011).
- [45] N. E. Hussey, J. Buhot, and S. Licciardello, *Rep. Prog. Phys.* **81**, 052501 (2018).
- [46] Y. Kuwata, H. Kotegawa, H. Sugawara, T. Sakurai, H. Ohta, and H. Tou, *J. Phys. Soc. Jpn.* **87**, 073703 (2018).
- [47] P. O. Sprau, A. Kostin, A. Kreisel, A. E. Böhmer, V. Taufour, P. C. Canfield, S. Mukherjee, P. J. Hirschfeld, B. M. Andersen, and J. C. Séamus Davis, *Science* **357**, 75 (2017).
- [48] Y. Nakajima, Z. Mita, H. Watanabe, Y. Ohtsubo, T. Ito, H. Kotegawa, H. Sugawara, H. Tou, and S. I. Kimura, *Phys. Rev. B* **100**, 125151 (2019).
- [49] T. Egami and S. J. L. Billinge, *Underneath the Bragg Peaks: Structural Analysis of Complex Materials*, 2nd ed. (Elsevier, Amsterdam, 2012).
- [50] T. Weber and A. Simonov, *Z. Kristallogr.* **227**, 238 (2012).
- [51] H. Goto, T. Toriyama, T. Konishi, and Y. Ohta, *Phys. Procedia* **75**, 91 (2015).
- [52] D. Ootsuki, K. Sawada, H. Goto, D. Hirai, D. Shibata, M. Kawamoto, A. Yasui, E. Ikenaga, M. Arita, H. Namatame *et al.*, *Phys. Rev. B* **101**, 165113 (2020).
- [53] Z. Fisk and J. P. Remeika, in *Handbook on the Physics and Chemistry of Rare Earths* edited by K. A. Gschneidner Jr. and L. Eyring (Elsevier, Amsterdam, 1989), Vol. 12, pp. 53–70.
- [54] P. J. Chupas, X. Qiu, J. C. Hanson, P. L. Lee, C. P. Grey, and S. J. L. Billinge, *J. Appl. Crystallogr.* **36**, 1342 (2003).
- [55] G. Ashiotis, A. Deschildre, Z. Nawaz, J. P. Wright, D. Karkoulis, F. E. Picca, and J. Kieffer, *J. Appl. Crystallogr.* **48**, 510 (2015).
- [56] P. Juhás, T. Davis, C. L. Farrow, and S. J. L. Billinge, *J. Appl. Crystallogr.* **46**, 560 (2013).
- [57] C. L. Farrow, P. Juhás, J. Liu, D. Bryndin, E. S. Božin, J. Bloch, T. Proffen, and S. J. L. Billinge, *J. Phys.: Condens. Matter* **19**, 335219 (2007).
- [58] P. Juhás, C. L. Farrow, X. Yang, K. R. Knox, and S. J. L. Billinge, *Acta Crystallogr., Sect. A: Found. Adv.* **71**, 562 (2015).
- [59] I. Jeong, T. Proffen, F. Mohiuddin-Jacobs, and S. J. L. Billinge, *J. Phys. Chem. A* **103**, 921 (1999).

- [60] R. J. Koch, N. Roth, Y. Liu, O. Ivashko, A. Dippel, C. Petrovic, B. B. Iversen, M. v. Zimmermann, and E. S. Bozin, *Acta Crystallogr., Sect. A: Found. Adv.* **77**, 611 (2021).
- [61] G. Kresse and J. Hafner, *Phys. Rev. B* **47**, 558 (1993).
- [62] P. E. Blöchl, *Phys. Rev. B* **50**, 17953 (1994).
- [63] J. P. Perdew, K. Burke, and M. Ernzerhof, *Phys. Rev. Lett.* **77**, 3865 (1996).
- [64] V. Popescu and A. Zunger, *Phys. Rev. B* **85**, 085201 (2012).
- [65] See <https://github.com/QijingZheng/VaspBandUnfolding>.
- [66] See Supplemental Material at <http://link.aps.org/supplemental/10.1103/PhysRevB.106.214516> for technical details of the analysis and additional experimental evidence supporting the main observations of local and average structure behaviors.
- [67] M. J. Krogstad, S. Rosenkranz, J. M. Wozniak, G. Jennings, J. P. C. Ruff, J. T. Vaughey, and R. Osborn, *Nat. Mater.* **19**, 63 (2020).
- [68] L. Yang, R. J. Koch, H. Zheng, J. F. Mitchell, W. Yin, M. G. Tucker, S. J. L. Billinge, and E. S. Bozin, *Phys. Rev. B* **102**, 235128 (2020).
- [69] R. J. Koch, R. Sinclair, M. T. McDonnell, R. Yu, M. Abeykoon, M. G. Tucker, A. M. Tselik, S. J. L. Billinge, H. D. Zhou, W.-G. Yin *et al.*, *Phys. Rev. Lett.* **126**, 186402 (2021).
- [70] C. F. van Bruggen, R. J. Haange, G. A. Wiegers, and D. K. G. de Boer, *Physica B+C* **99**, 166 (1980).
- [71] S. Kobayashi, N. Katayama, T. Manjo, H. Ueda, C. Michioka, J. Sugiyama, Y. Sassa, O. K. Forsslund, M. Månsson, K. Yoshimura *et al.*, *Inorg. Chem.* **58**, 14304 (2019).
- [72] D. Hirai, K. Kojima, N. Katayama, M. Kawamura, D. Nishio-Hamane, and Z. Hiroi, *J. Am. Chem. Soc.* **144**, 17857 (2022).
- [73] V. K. Anand, D. T. Adroja, M. R. Lees, P. K. Biswas, A. D. Hillier, and B. Lake, *Phys. Rev. B* **98**, 214517 (2018).
- [74] L. Taillefer, *Annu. Rev. Condens. Matter Phys.* **1**, 51 (2010).
- [75] S. Badoux, W. Tabis, F. Laliberté, G. Grissonnanche, B. Vignolle, D. Vignolles, J. Béard, D. A. Bonn, W. N. Hardy, R. Liang *et al.*, *Nature (London)* **531**, 210 (2016).